Science Bulletin 70 (2025) 882–888

Contents lists available at ScienceDirect

Science Bulletin

journal homepage: www.elsevier.com/locate/scib

Article

Abrupt lateral beam shifts from terahertz quasi-bound states in the continuum

Minggui Wei[a], Yang Long[a,*], Feng Wu[b,*], Gui-Geng Liu[a], Baile Zhang[a,c,*]

[a] Division of Physics and Applied Physics, School of Physical and Mathematical Sciences, Nanyang Technological University, Singapore 637371, Singapore
[b] School of Optoelectronic Engineering, Guangdong Polytechnic Normal University, Guangzhou 510665, China
[c] Centre for Disruptive Photonic Technologies, The Photonics Institute, Nanyang Technological University, Singapore 639798, Singapore

ARTICLE INFO

Article history:
Received 13 August 2024
Received in revised form 15 November 2024
Accepted 30 December 2024
Available online 9 January 2025

Keywords:
Bound states in the continuum
Lateral shifts
Terahertz optics

ABSTRACT

Bound states in the continuum (BICs) are notable in photonics for their infinite *Q* factors. Perturbed BICs, or quasi-BICs (QBICs), have finite but ultra-high *Q* factors, enabling external coupling. So far, most studies have focused on the momentum-space properties of BICs and QBICs, with few discussions on their properties in real space. Here, we experimentally demonstrate that QBICs can induce abrupt lateral beam shifts. By applying Brillouin zone folding to a compound grating waveguide, we form a QBIC band where all states become QBICs. When excited at specific incident angles, these QBICs produce sudden lateral beam shifts, rapidly disappearing as frequencies deviate from the QBIC band. Using terahertz imaging, we capture these beam shifts at different incident angles, characterizing the QBIC band. This work offers alternative insights into QBIC behaviors and supports the development of advanced sensors and wavelength division (de) multiplexers.

1. Introduction

Bound states in the continuum (BICs) lie inside the continuum, perfectly confine without any radiation, and exhibit infinite *Q* factors, thereby garnering remarkable attention in photonics [1–4]. With slight perturbations, BICs that are unresponsive to external incidence can evolve into quasi-BICs (QBICs), which exhibit finite but ultra-high *Q* factors, enabling external coupling [5–10]. QBICs have been extensively utilized for unidirectional guided resonance [11], intrinsic chirality [12–14], complete polarization conversion [15,16], and others [17–21]. So far, considerable research on QBICs is mostly focused on their corresponding BICs' momentum-space properties [22–25], such as polarization vortices or topological charges defined in momentum space. However, studies have shown that momentum-space polarization vortices can be absent in QBICs or certain types of BICs [26], prompting explorations of QBICs' real-space properties, such as beam shifts [27,28].

Real-space shifts of light beams occur at interfaces between different media [29–32], manifesting as lateral shifts (LSs) [33] and transverse shifts (TSs) [34,35]. LSs, including Goos-Hänchen shifts, have been extensively studied in optical systems such as subwavelength gratings [36], waveguides [37], multilayers [38,39], and photonic crystals [40–43], and have also been predicted and observed in electronic systems [44–46]. From the perspective of the physical mechanism, the enhancement of the LSs in Refs. [36–43] originates from the conventional bound states with discrete frequencies, such as Fabry-Perot cavities and Bloch surface modes. LSs typically depend on the strength of light-matter interactions, thereby serving as a measure of these interactions [41,43]. Given the high-*Q* factors of QBICs, which indicate strong light-matter interactions, understanding the interplay between QBICs and LSs remains an important area for experimental discussions.

Here, we report the experimental demonstration of QBIC-induced abrupt LSs of a terahertz beam. Using a compound grating waveguide with a folded Brillouin zone, we establish a QBIC band where all states become QBICs. Significant LSs emerge across a wide range of incident angles when the frequency falls within the QBIC band; these shifts rapidly vanish with slight deviations in frequency or angle, as illustrated in Fig. 1. We capture these shifts with a terahertz field-scanning imaging system, introducing a novel method for QBIC band characterization. Notably, at an incident angle of 21°, we observe a maximum LS of 41.16 times the wavelength at 1.0774 THz, nearly 3.35 times larger than previously reported LSs in the terahertz regime [47–49] (Note S1 online). Our findings provide fresh insights into the real-space behaviors of QBICs and pave the way for developing high-efficiency LS-based devices such as advanced sensors and wavelength division (de)multiplexers.

---

* Corresponding authors.
E-mail addresses: yang.long@ntu.edu.sg (Y. Long), fengwu@gpnu.edu.cn (F. Wu), blzhang@ntu.edu.sg (B. Zhang).

https://doi.org/10.1016/j.scib.2025.01.006
2095-9273/

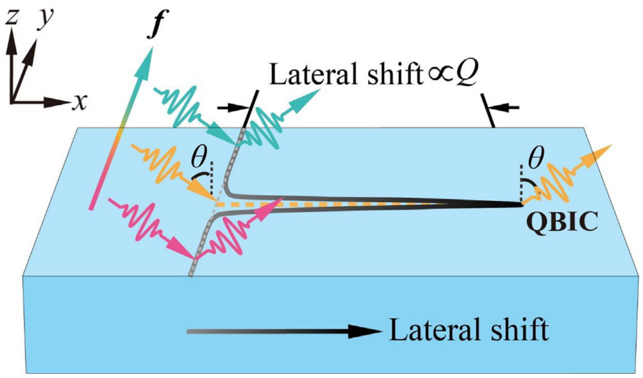

Fig. 1. Schematic of the abrupt LS induced by the QBIC. When a broadband pulse is incident onto an optical interface hosting QBICs, the reflected beam at the QBIC frequency can exhibit a significant LS at a specific incident angle, θ. This LS is directly related to the Q factor of the QBIC. As the frequency or incident angle slightly deviates from the QBIC conditions, the LS rapidly diminishes.

2. Methods

To schematically describe the unit cell of the proposed compound grating waveguide, Fig. 2a illustrates a configuration comprising a silicon (Si) grating layer and a Si waveguide layer. The Si grating layer is characterized by a dual-period grating layer with a period P = 120 μm and a thickness h = 35 μm. The widths of adjacent Si ridges are identical, denoted as $w_H = 0.275P$. In contrast, the widths of adjacent air grooves vary, denoted as $w_{L1} = 0.225P(1-\delta w)$ and $w_{L2} = 0.225P(1+\delta w)$, respectively. Here, $\delta w \in [-1, 1]$ represents a tunable geometric parameter indicating the width difference between these two adjacent air grooves. The Si waveguide layer has a thickness of t = 480 μm, and the refractive index of Si is $n_{Si} = 3.42$.

Here, we consider a TE-polarized (electric field parallel to the y-direction) light incident onto the compound grating waveguide at an incident angle θ. In the case of $\delta w \neq 0$, the grating layer is a dual-period structure with a period of P. According to the guided mode resonance theory, the momentum-matching condition is given by [27,50]

$$K_{x,i} = k_0\sin\theta - i\frac{2\pi}{P} = \beta_m \quad (i = \pm1, \pm2, \cdots), \tag{1}$$

where $K_{x,i}$ represents the tangential component of the wavevector in the dual-period grating layer, $k_0 = 2\pi/\lambda_0$ is the wave vector in air with the wavelength λ_0 in air, i is the diffraction order, $2\pi/P$ is the reciprocal lattice vector, and β_m is the propagation constant of the TE$_m$ mode in the waveguide layer. For simplicity, we ignore the band distortion induced by the Bloch scattering of the grating layer (Note S2 online). Eq. (1) is applicable to all guided mode orders; we specifically focus on the TE$_9$ guided mode. Fig. 2b depicts the folded dispersion relation of the TE$_9$ guided mode, with the first Brillouin zone boundary at $k_x = \pi/P$. When normally incident light interacts with the compound grating waveguide, the tangential wavevector component in the grating layer for the –1st order diffraction is $K_{x,-1} = 2\pi/P$. The momentum-matching condition $K_{x,-1} = 2\pi/P = \beta_9$ predicts a momentum-matching point denoted by A (at 1.0886 THz) in Fig. 2b. For the –2nd order diffraction, $K_{x,-2} = 4\pi/P = \beta_9$, presenting a momentum-matching point denoted by B (at 1.6766 THz). At these two momentum-matching points, the TE$_9$ guided modes are excitable, giving rise to two Fano resonances.

In the case of $\delta w = 0$, the grating layer reduces to a mono-period grating with a period of $P' = P/2$. The reciprocal lattice vector doubles accordingly. Thus, the momentum-matching condition turns into

$$K'_{x,i'} = k_0\sin\theta - i'\frac{2\pi}{P'} = k_0\sin\theta - i'\frac{4\pi}{P} = \beta_m \quad (i' = \pm1, \pm2, \cdots), \tag{2}$$

where $K'_{x,i'}$ represents the tangential component of the wavevector in the mono-period grating layer, and i' denotes the diffraction order. Fig. 2c gives the folded dispersion relation of the TE$_9$ guided mode. With the grating period halved, the first Brillouin zone boundary becomes $k_x = \pi/P' = 2\pi/P$. When normally incident light interacts with the compound grating waveguide, the tangential component of the wavevector in the mono-period grating layer for the –1st order diffraction is $K'_{x,-1} = 4\pi/P$, identical to the –2nd order diffraction in the dual-period grating layer $K_{x,-2} = 4\pi/P$. Consequently, only the momentum-matching point B (at 1.6766 THz) remains excitable. As the geometric parameter δw changes from a non-zero value to zero, the guided mode at point A switches from being excitable to unexcitable due to momentum mismatch. Such an unexcitable mode at point A in the case of $\delta w = 0$ is termed a momentum-mismatch-driven BIC, while the excitable mode at point A in the case of $\delta w \neq 0$ is referred to as a momentum-mismatch-driven QBIC [50]. Note that $\delta w = 0$ causes a discrete change in the lattice constant compared to cases where $\delta w \neq 0$, resulting in a discontinuous variation in the size of the Brillouin zone. Similarly, the Q factor of the QBICs should exhibit a discontinuous dependence on δw. The Q factor near the discontinuity at $\delta w = 0$ can be evaluated as $\lim_{\delta w \to 0} Q = \infty$, implying that QBICs on the QBIC band can transition into BICs. In contrast, the guided mode at point B remains consistently excitable, leading to a conventional Fano resonance with a finite Q factor.

As the incident angle can be mapped to the tangential wavevector in momentum space, sweeping the angle θ from 0° to 90° shifts the position of the momentum-mismatch-driven QBIC (i.e., point A with $\theta = 0°$) across momentum space, delineating the QBIC bands illustrated by the pink lines in Fig. 2b. Correspondingly, the position of the conventional Fano resonance (i.e., point B with $\theta = 0°$) in both cases of $\delta w \neq 0$ and $\delta w = 0$ shifts across momentum space, forming the conventional Fano bands, as shown by the orange lines in Fig. 2b and c. Comparing Fig. 2c with Fig. 2b, the bands in the momentum region $\pi/P \leq k_x \leq 2\pi/P$ in the case of $\delta w = 0$ fold into the momentum region $0 \leq k_x \leq \pi/P$ in the case of $\delta w \neq 0$, thereby forming QBIC bands. Unlike symmetry-protected and accidental QBICs found within narrow incident angle ranges [5], momentum-mismatch-driven QBICs are situated across wide incident angle ranges.

Next, we investigate the real-space behavior of the momentum-mismatch-driven QBICs. When a light beam is obliquely incident onto the compound grating waveguide and induces the waveguide mode with a non-zero group velocity ($v_g \neq 0$), the LS at the surface can be estimated as $L = v_g\tau$, where τ denotes the lifetime. It is known that the Q factor is defined as $Q = 2\pi f_0\tau$, where f_0 is the resonance frequency. The lifetime τ is associated with losses arising from two parts: the radiation loss τ_r and the dielectric loss τ_d, namely $\tau^{-1} = \tau_r^{-1} + \tau_d^{-1}$. The dielectric losses from the silicon grating and waveguide slab are quite small and can be ignored in the terahertz regime. Therefore, we consider that $\tau \approx \tau_r$. Combining with the definition of Q factor, we finally have $L = v_g Q/(2\pi f_0)$. This implies that the LS is proportional to the Q factor. As illustrated in Fig. 1, an abrupt LS emerges at the QBIC frequency with an ultrahigh Q factor. Conversely, the LS nearly vanishes when the frequency deviates from the QBIC frequency. Driven by the QBIC band, abrupt LS can be observed over a wide range of incident angles.

Fig. 2d illustrates the dependences of the QBIC's Q factor on the inverse quadratic of the geometric parameter δw for different incident angles θ = 14°, 15.75°, 17.5°, 19.25°, and 21°, respectively. The circles denote the simulated Q factors, while solid lines depict the corresponding linear fitting curves. The Q factor of a QBIC is known

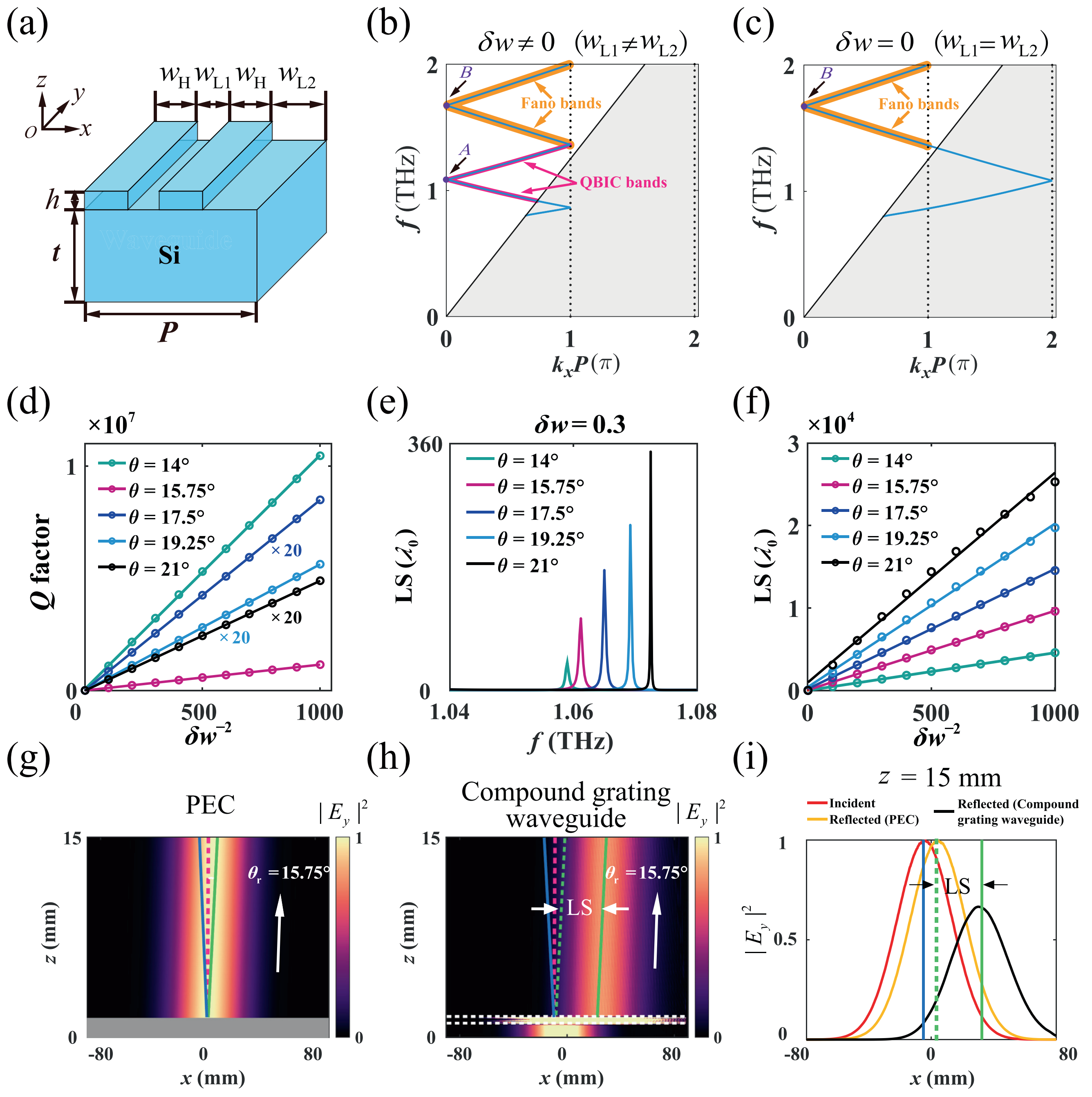

Fig. 2. Schematic of QBIC bands and LSs induced by QBIC bands. (a) Schematic of a unit cell of the compound grating waveguide. Folded dispersion relations of the TE_9 guided mode in the waveguide layer for the dual-period (b) and mono-period gratings (c). The red and orange lines represent the QBIC bands and Fano bands, respectively. (d) Dependences of the Q factor of the QBIC on the inverse quadratic of the geometric parameter δw^{-2} for different incident angles θ = 14°, 15.75°, 17.5°, 19.25°, and 21°, respectively. The circles denote the simulated Q factors. The solid lines denote the linear fitting curves. (e) Dependences of the calculated LSs on the frequency for different incident angles θ = 14°, 15.75°, 17.5°, 19.25°, and 21° with the geometric parameter δw = 0.3, respectively. (f) Dependences of the maximum LS on the inverse quadratic of the geometric parameter δw^{-2} for different incident angles θ = 14°, 15.75°, 17.5°, 19.25°, and 21°, respectively. (g) The electric field intensity distribution of the beam reflected by a PEC (the gray region) at an incident angle of θ = 15.75° at 1.0644 THz. The blue lines represent the average centers of the incident beams. The red dashed lines represent the normal lines of the interface between a grating waveguide and air. (h) The electric field intensity distribution of the beam reflected by the compound grating waveguide at an incident angle of θ = 15.75° at 1.0644 THz. The region between two white dashed lines represents the compound grating waveguide structure. The green dashed and solid lines represent the average centers of the beams reflected by the PEC and compound grating waveguide structure, respectively. (i) The electric field intensity distributions of the incident beam, the reflected beam by PEC, and the reflected beam by the compound grating waveguide at a height of z = 15 mm, respectively.

to be proportional to the inverse quadratic of the geometric parameter δw [5,51], a relationship consistent across different incident angles. As previously discussed, the QBIC band enables the observation of abrupt LSs across a range of incident angles. Fig. 2e shows the frequency-dependent behavior of LSs for incident angles θ = 14°, 15.75°, 17.5°, 19.25°, and 21° with the geometric parameter δw = 0.3, as calculated by the stationary phase approach [52]. Abrupt LSs emerge precisely at the QBIC frequencies under specific incident angles, sharply decreasing to near zero with slight deviations from the corresponding QBIC frequencies, attributable to the QBIC band's effect. In Fig. 2f, the dependence of calculated maximum LSs on the inverse quadratic of the geometric parameter δw is presented for different incident angles θ = 14°, 15.75°, 17.5°, 19.25°, and 21°. Circles indicate calculated maximum LSs, with solid lines representing corresponding linear fits. These maximum LSs scale proportionally with the inverse quadratic of δw, namely, LS $\propto \delta w^{-2}$. Thus, as the Q factor of the QBIC approaches infinity, the LS also approaches infinity exclusively at the QBIC frequency, while LSs at other frequencies diminish to nearly zero.

Next, we numerically simulate the LS in the case of a Gaussian beam incidence (Note S3 online). The incident angle is 15.75°, corresponding to a QBIC frequency of 1.0644 THz. The beam waist is approximately $170.30\lambda_0$ (48 mm). Fig. 2g and h display the intensity distribution of the beam reflected by a perfect electric conductor (PEC) and by the proposed compound grating waveguide with a geometric parameter $\delta w = 0.3$, respectively. Red dashed lines represent the normal lines of the interface between the PEC or grating waveguide and air. In Fig. 2g, the blue and green lines indicate the average center of the incident beam and the beam reflected by the PEC, respectively (Note S3 online). In Fig. 2h, the region between two white dashed lines indicates the position of the compound grating waveguide. The average centers of the reflected beams for the PEC and compound grating waveguide are indicated by the green dashed and solid lines, respectively. The LS is determined by calculating the distance between the green dashed and solid lines at the height of $z = 15$ mm, as shown in Fig. 2i. The simulated LS is approximately 28.12 mm ($\sim 99.48\lambda_0$), slightly smaller than the LS calculated using the stationary phase approach, which is 29.74 mm ($\sim 105.21\lambda_0$).

3. Experiments and discussion

We fabricate a compound grating waveguide with a geometric parameter $\delta w = 0.3$ by etching a Si wafer. Fig. 3a depicts a schematic of a 4-f terahertz time-domain system, and Fig. 3b shows a microscope image of the sample, highlighting the different widths of two adjacent air grooves in a unit cell. Fig. 3c presents the simulated and measured angular transmittance spectra of the compound grating waveguide, where the transmittance dips reveal the QBIC bands. The measured spectrum aligns well with the simulated one, although a slight deviation from the two dispersion relations of the TE_9 guided mode in Fig. 2c is observed due to the Bloch scattering of the grating layer (Note S2 online) [21]. The limited frequency resolution of the system causes the measured line widths of the QBIC bands to be larger than those simulated (Note S4 online). The wave-like nature of the QBIC bands indicates both positive and negative group velocities, resulting in corresponding positive and negative LSs (Note S3 online). Specifically, for the upper QBIC band (with frequencies ranging from 1.05 to 1.08 THz), the group velocities are negative for incident angles ranging from ∼8° to ∼13° or greater than 22°, resulting in negative LSs. Due to the real-space measurement restrictions, we focus on measuring the abrupt positive LSs induced by QBICs within the incident angle range of 13° to 22°.

To experimentally observe the abrupt LSs, we utilize a terahertz field-scanning imaging system, as shown in Fig. 4a. The translation stage, with a maximum travel range of 20 mm, provides a view of both incident and reflected beams. Different incident angles are achieved by rotating the sample. The directly measured spatial shifts (L_0) are determined through the spatial difference between the average center of the reflected beams along the x-direction and then transformed to obtain the corresponding LSs (Note S4 online). Fig. 4b–j illustrate the measured electric field intensity distributions of the reflected beams from 1.0481 to 1.0881 THz,

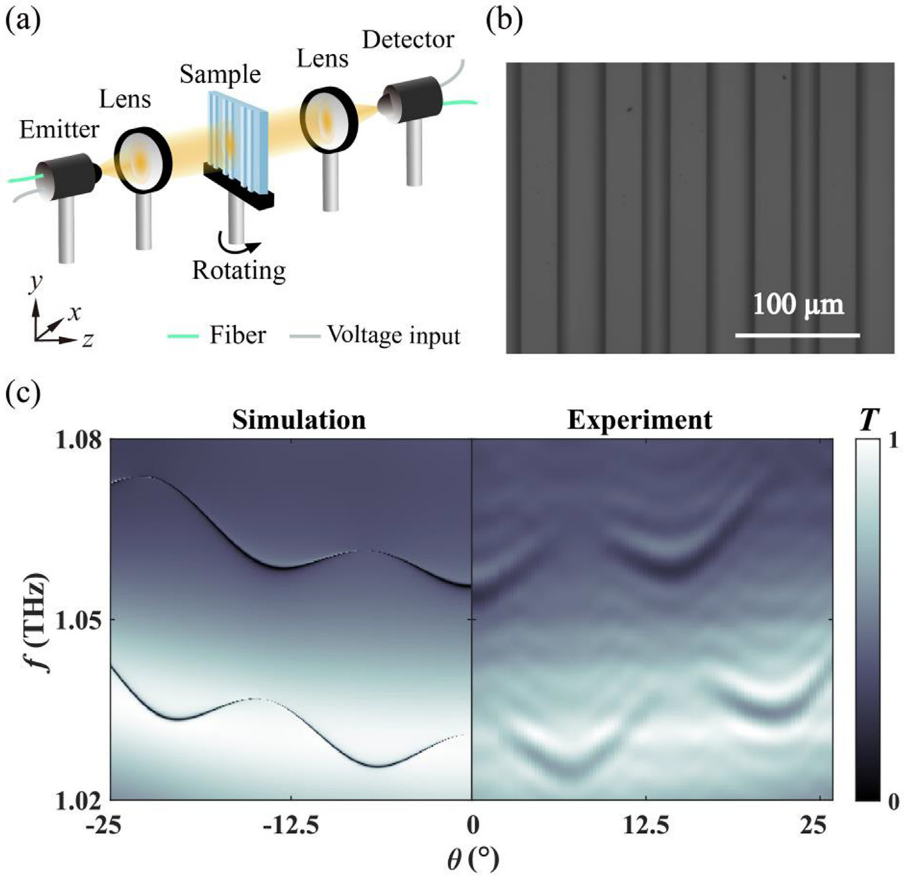

Fig. 3. Angular transmittance spectra of the compound grating waveguide. (a) Schematic of a 4-f terahertz time-domain system. (b) Microscope image of the compound grating waveguide with a geometric parameter $\delta w = 0.3$. (c) Simulated and measured angular transmittance spectra of the compound grating waveguide.

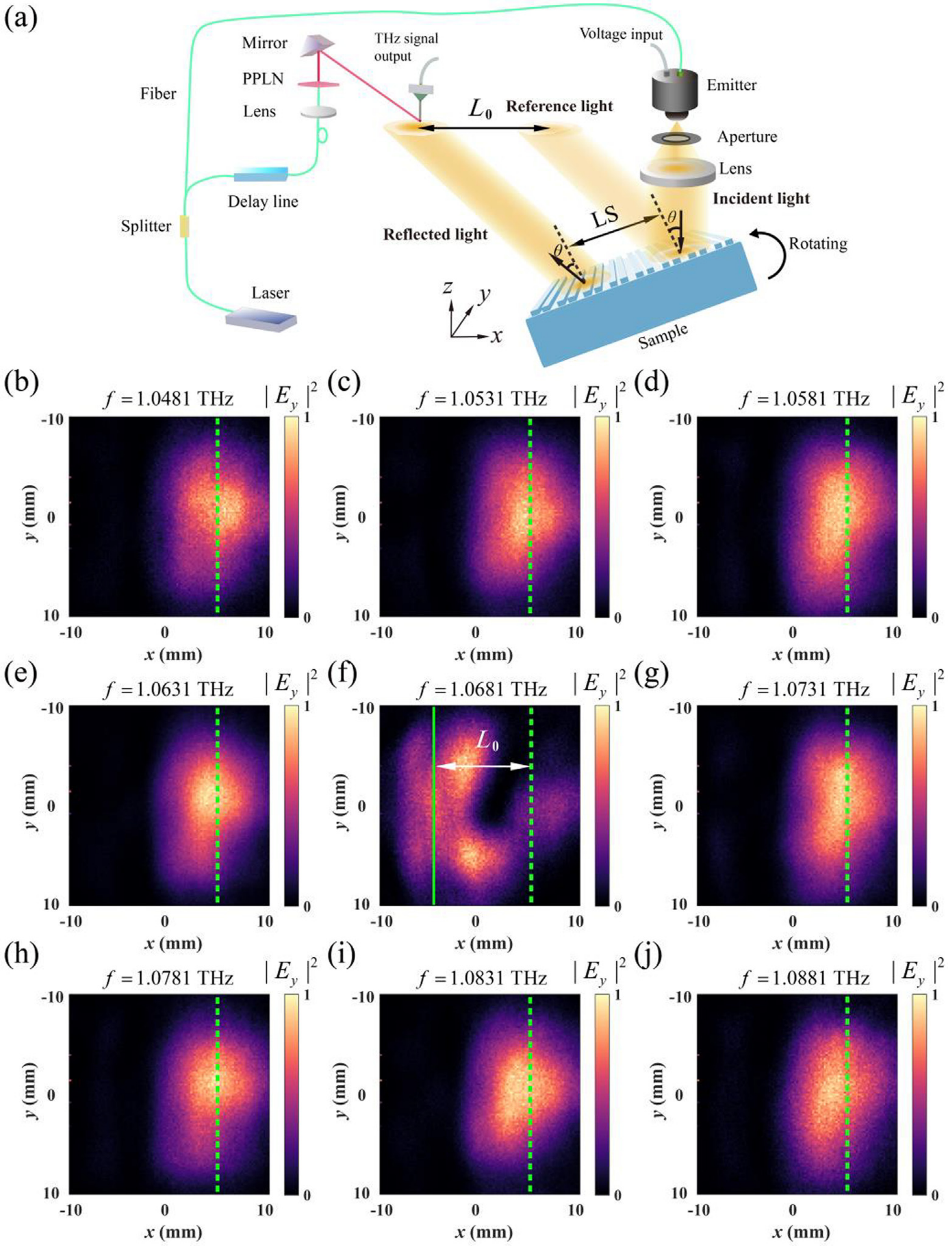

Fig. 4. Measured LS under an incident angle of 17.5°. (a) Schematic of the terahertz field-scanning imaging system for the measurement of LSs. Periodically poled lithium niobate (PPLN). (b–j) Measured electric field intensity distributions of the reflected beams from 1.0481 to 1.0881 THz with an increment of 0.005 THz under an incident angle of 17.5°, respectively. The green solid lines and green dashed lines represent the measured average centers of the reflected beams for working and reference frequencies (1.050 THz), respectively. The electric field intensity distributions are normalized by the maximum value of the electric field intensity distributions in the corresponding figures.

with an increment of 0.005 THz at an incident angle of 17.5°. The green dashed lines in Fig. 4b–j indicate the average center of the reflected beam at 1.050 THz (Note S5 online). Since 1.050 THz deviates from the QBIC frequency at 17.5°, its LS is zero, making it a reference position. At 1.0681 THz, the average center of the reflected beam shifts significantly along the −*x*-direction, marked by the green solid line, indicating a substantial LS, as illustrated in Fig. 4f. The L_0 at 1.0681 THz is approximately 9.90 mm, corresponding to an LS of about 8.50 mm (~30.26λ_0). In contrast, the average centers of the reflected beams for frequencies from 1.0481 to 1.0631 THz are nearly aligned with the green dashed line in Fig. 4b–e, indicating near-zero LSs. Similarly, the LSs are near zero for the reflected beams for frequencies ranging from 1.0731 to 1.0881 THz, as illustrated in Fig. 4g–j.

The measured LSs from 1.05 to 1.09 THz are shown in Fig. 5a. The frequency range of the significant LSs is 0.0075 THz, which is only 0.7% of the QBIC frequency. The measured results demonstrate that an LS induced by a QBIC is highly sensitive to frequency changes under a specific incident angle, rapidly decreasing to near zero when the frequency deviates from the QBIC frequency, as illustrated in Fig. 1.

We measured LSs at incident angles ranging from 13° to 21°, which excite QBICs with positive group velocities (the upper QBIC band in Fig. 3c). Interestingly, the group velocity of the QBIC

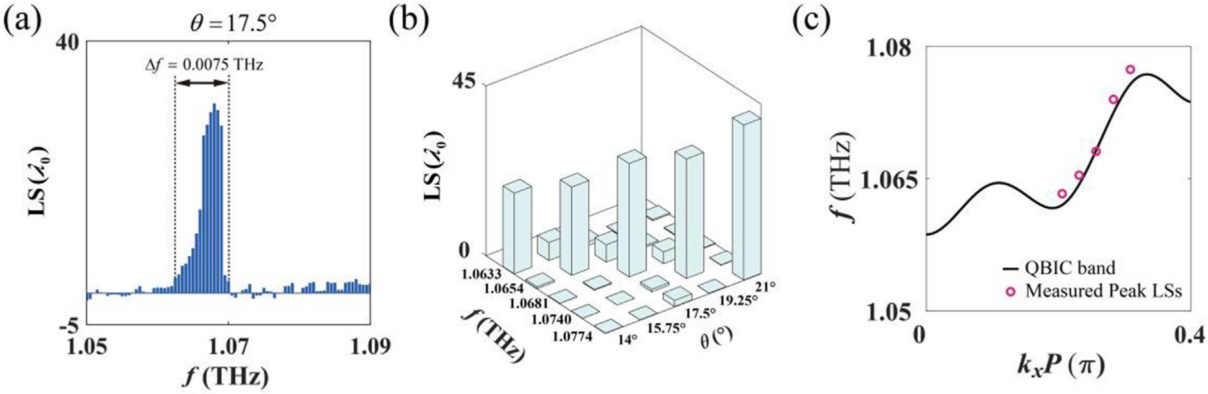

Fig. 5. Measured LSs under different incident angles and the retrieved QBIC band. (a) The measured LSs of different frequencies at an incident angle of 17.5°. (b) Measured LSs at five QBICs' frequencies corresponding to incident angles θ = 14°, 15.75°, 17.5°, 19.25°, and 21°, respectively. (c) The upper QBIC band of the compound grating waveguide (black line) and the frequencies of the measured peak LSs under different incident angles (red circles).

approaches zero at an incident angle of 13°, resulting in an LS of nearly zero across the frequency range (Note S3 online). This is an exceptional case of the abrupt LSs induced by QBIC. Abrupt LSs are observed at incident angles ranging from 14° to 21°. Fig. 5b illustrates the measured LSs at five QBICs' frequencies corresponding to incident angles θ = 14°, 15.75°, 17.5°, 19.25°, and 21°, respectively. Typically, when the incident angle deviates from 17.5°, the measured abrupt LS at 1.0681 THz (QBIC frequency corresponding to the incident angle of 17.5°) drops from $\sim 30.26\lambda_0$ to near zero. Thus, the abrupt LSs induced by QBICs are sensitive to both frequencies and incident angles.

The frequencies of the measured peak LSs under different incident angles can reveal the QBIC band of the compound grating waveguide, as shown in Fig. 5c. Real-space measurements of LSs can reveal QBIC bands in momentum space, providing an alternative method to characterize QBICs. Given that LSs are nearly zero with only a 0.47% frequency deviation from QBICs, real-space measurement offers high precision in characterizing QBICs. Generally, the entire QBIC band of the compound grating waveguide can be reconstructed by measuring abrupt LSs over a wide range of incident angles, including those below ~13° and above ~22°. The LS measurements at these incident angles are limited by our current experimental setup (Note S4 online).

Owing to the limited Gaussian-like beam size of the incident terahertz beam and imperfections in its profile, the measured LSs are smaller than the simulated LSs (Note S6 online). The difference can be minimized by increasing the beam waist of the incident terahertz beam. In our work, significant LSs remain observable, consistent with simulations, and in alignment with the measured transmission spectra. Notably, the measured maximum LS reaches 41.16 times the wavelength at 1.0774 THz with an incident angle of 21°, which is nearly 3.35 times larger than those reported in previous works in the terahertz regime [47–49]. Without the requirement of high power or high temperature, the abrupt LSs introduced by the QBICs may have applications in developing ultra-sensitive sensors, filters, and multiplexers for terahertz systems.

Although some prior studies address related topics, such as beam shifts around BICs [28] and the formation of BICs through band folding [24], they primarily focus on BICs rather than the QBICs investigated in our work. It should be noted that the main point of this work is distinct from those in Refs. [27,50,53]. In Ref. [27], the researchers enhanced lateral beam shifts based on QBICs. Nevertheless, Ref. [27] is a theoretical work in the near-infrared regime. In addition, in Ref. [27], the researchers only noticed a QBIC in a compound grating waveguide at a specific incident angle. In this work, we theoretically and experimentally reveal a QBIC band consisting of continuous QBICs in a compound grating waveguide in the terahertz regime. In Ref. [50], the researchers elucidated the formation of BICs in compound grating waveguides from the perspective of momentum mismatch. Nevertheless, Ref. [50] did not discuss lateral beam shifts. In our work, we reveal the relationship between abrupt lateral beam shifts and QBIC bands. In Ref. [53], the researchers theoretically discuss the enhancement of lateral beam shifts based on defect modes in one-dimensional photonic crystals containing dielectric defects. The lateral beam shifts are enhanced by conventional bound states with discrete frequencies. In this work, we theoretically and experimentally enhanced lateral beam shifts by QBIC bands.

4. Conclusion

In conclusion, we experimentally demonstrate abrupt LSs induced by QBICs in a compound grating waveguide at terahertz frequencies. By exploiting the Brillouin zone folding, we obtain QBIC bands. To observe the abrupt LSs induced by the QBICs, we employ a terahertz field-scanning imaging system. At specific incident angles, the LSs emerge at the QBIC frequency and drop to zero with a frequency deviation of only 0.47% from the QBIC frequency. We experimentally observe abrupt LSs over a range of incident angles. The real-space measurement of LSs can provide an alternative characterization of QBICs. These results not only provide new insights into the real-space characteristics of QBICs but also advance the development of LS-based devices, such as high-performance sensors and wavelength division (de)multiplexers.

Conflict of interest

The authors declare that they have no conflict of interest.

Acknowledgments

This work was supported by the Singapore National Research Foundation Competitive Research Program (NRF-CRP23-2019-0007) and the Singapore Ministry of Education Academic Research Fund Tier 2 (MOE-T2EP50123-0007). Feng Wu acknowledges support from the National Natural Science Foundation of China (12104105) and Guangdong Basic and Applied Basic Research Foundation (2023A1515011024). Yang Long gratefully acknowledges the support of the Eric and Wendy Schmidt AI in Science Postdoctoral Fellowship, a Schmidt Futures program.

Author contributions

Yang Long and Feng Wu proposed the idea. Minggui Wei, Yang Long, and Feng Wu designed the samples. Minggui Wei and Gui-Geng Liu performed the optical measurement and data analysis. Minggui Wei and Gui-Geng Liu organized the manuscript. Yang Long, Feng Wu, and Baile Zhang supervised the work. All authors contributed to the writing and revision of the manuscript.

Appendix A. Supplementary material

Supplementary data to this article can be found online at https://doi.org/10.1016/j.scib.2025.01.006.

References

[1] Hsu CW, Zhen B, Stone AD, et al. Bound states in the continuum. Nat Rev Mater 2016;1:16048.
[2] Sadreev AF. Interference traps waves in an open system: bound states in the continuum. Rep Prog Phys 2021;84:055901.
[3] Kang M, Liu T, Chan CT, et al. Applications of bound states in the continuum in photonics. Nat Rev Phys 2023;5:659–78.
[4] Wang J, Li P, Zhao X, et al. Optical bound states in the continuum in periodic structures: mechanisms, effects, and applications. Photon Insights 2024;3:R01.
[5] Koshelev K, Lepeshov S, Liu M, et al. Asymmetric metasurfaces with high-*Q* resonances governed by bound states in the continuum. Phys Rev Lett 2018;121:193903.
[6] Kim S, Kim K-H, Cahoon JF. Optical bound states in the continuum with nanowire geometric superlattices. Phys Rev Lett 2019;122:187402.
[7] Feng S, Liu T, Chen W, et al. Enhanced sum-frequency generation from etchless lithium niobate empowered by dual quasi-bound states in the continuum. Sci China Phys Mech Astron 2023;66:124214.
[8] Jin J, Yin X, Ni L, et al. Topologically enabled ultrahigh-*Q* guided resonances robust to out-of-plane scattering. Nature 2019;574:501–4.
[9] Sun K, Wei H, Chen W, et al. Infinite-*Q* guided modes radiate in the continuum. Phys Rev B 2023;107:115415.
[10] Chai R, Liu Q, Liu W, et al. Emerging planar nanostructures involving both local and nonlocal modes. ACS Photonics 2023;10:2031–44.
[11] Yin X, Jin J, Soljačić M, et al. Observation of topologically enabled unidirectional guided resonances. Nature 2020;580:467–71.
[12] Gorkunov MV, Antonov AA, Kivshar YS. Metasurfaces with maximum chirality empowered by bound states in the continuum. Phys Rev Lett 2020;125:093903.
[13] Chen Y, Deng H, Sha X, et al. Observation of intrinsic chiral bound states in the continuum. Nature 2023;613:474–8.
[14] Chen Y, Chen W, Kong X, et al. Can weak chirality induce strong coupling between resonant states? Phys Rev Lett 2022;128:146102.
[15] Guo Y, Xiao M, Fan S. Topologically protected complete polarization conversion. Phys Rev Lett 2017;119:167401.
[16] Chen F, Gao Z, Zhang L, et al. Observation of topologically enabled complete polarization conversion. Laser Photonics Rev 2023;17:2200626.
[17] Carletti L, Koshelev K, De Angelis C, et al. Giant nonlinear response at the nanoscale driven by bound states in the continuum. Phys Rev Lett 2018;121:033903.
[18] Yu Z, Sun X. Acousto-optic modulation of photonic bound state in the continuum. Light Sci Appl 2020;9:1.
[19] Bulgakov EN, Sadreev AF. High-*Q* resonant modes in a finite array of dielectric particles. Phys Rev A 2019;99:033851.
[20] Zhao X, Huang R, Du X, et al. Ultrahigh-*Q* metasurface transparency band induced by collective–collective coupling. Nano Lett 2024;24:1238–45.
[21] Shi W, Gu J, Zhang X, et al. Terahertz bound states in the continuum with incident angle robustness induced by a dual period metagrating. Photon Res 2022;10:810–89.
[22] Wang B, Liu W, Zhao M, et al. Generating optical vortex beams by momentum-space polarization vortices centred at bound states in the continuum. Nat Photons 2020;14:623–8.
[23] Li H, Cao Y, Feng R, et al. Mode-symmetry-assisted optical pulling by bound states in the continuum. Phys Rev Lett 2024;132:253802.
[24] Wang W, Srivastava YK, Tan TC, et al. Brillouin zone folding driven bound states in the continuum. Nat Commun 2023;14:2811.
[25] Cotrufo M, Cordaro A, Sounas DL, et al. Passive bias-free non-reciprocal metasurfaces based on thermally nonlinear quasi-bound states in the continuum. Nat Photon 2024;18:81–90.
[26] Chai R, Liu W, Li Z, et al. Spatial information lasing enabled by full-*k*-space bound states in the continuum. Phys Rev Lett 2024;132:183801.
[27] Wu F, Wu J, Guo Z, et al. Giant enhancement of the Goos-Hänchen shift assisted by quasibound states in the continuum. Phys Rev Appl 2019;12:014028.
[28] Wang J, Shi L, Zi J. Spin Hall effect of light via momentum-space topological vortices around bound states in the continuum. Phys Rev Lett 2022;129:236101.
[29] Peccianti M, Dyadyusha A, Kaczmarek M, et al. Tunable refraction and reflection of self-confined light beams. Nat Phys 2006;2:737–42.
[30] Hosten O, Kwiat P. Observation of the spin Hall effect of light via weak measurements. Science 2008;319:787–90.
[31] Bliokh KY, Shadrivov IV, Kivshar YS. Goos–Hänchen and Imbert–Fedorov shifts of polarized vortex beams. Opt Lett 2009;34:389–91.
[32] Merano M, Aiello A, Van Exter MP, et al. Observing angular deviations in the specular reflection of a light beam. Nat Photon 2009;3:337–40.
[33] Goos F, Hänchen H. Ein neuer und fundamentaler Versuch zur Totalreflexion. Ann Phys 1947;436:333–46.
[34] Fedorov FI K. teroii polnogo otrazheniya. Dokl Akad Nauk SSSR 1955;105:465–8.
[35] Imbert C. Calculation and experimental proof of the transverse shift induced by total internal reflection of a circularly polarized light beam. Phys Rev D 1972;5:787–96.
[36] Yang R, Zhu W, Li J. Giant positive and negative Goos-Hänchen shift on dielectric gratings caused by guided mode resonance. Opt Express 2014;22:2043–50.
[37] Tsakmakidis KL, Boardman AD, Hess O. 'Trapped rainbow' storage of light in metamaterials. Nature 2007;450:397–401.
[38] Cao Y, Fu Y, Zhou Q, et al. Giant Goos-Hänchen shift induced by bounded states in optical PT-symmetric bilayer structures. Opt Express 2019;27:7857–67.
[39] Zhu S, Jaffiol R, Crunteanu A, et al. Label-free biosensing with singular-phase-enhanced lateral position shift based on atomically thin plasmonic nanomaterials. Light Sci Appl 2024;13:2.
[40] Felbacq D, Smaâli R. Bloch modes dressed by evanescent waves and the generalized Goos-Hänchen effect in photonic crystals. Phys Rev Lett 2004;92:193902.
[41] Soboleva IV, Moskalenko VV, Fedyanin AA. Giant Goos-Hänchen effect and Fano resonance at photonic crystal surfaces. Phys Rev Lett 2012;108:123901.
[42] Wang J, Zhao M, Liu W, et al. Shifting beams at normal incidence via controlling momentum-space geometric phases. Nat Commun 2021;12:6046.
[43] Du S, Zhang W, Liu W, et al. Realization of large transmitted optical Goos–Hänchen shifts in photonic crystal slabs. Nanophotonics 2022;11:4531–6.
[44] Renard RH. Total reflection: a new evaluation of the Goos–Hänchen shift. J Opt Soc Am 1964;54:1190–7.
[45] Carter JL, Hora H. Total reflection of matter waves: the Goos–Haenchen effect for grazing incidence. J Opt Soc Am 1971;61:1640–5.
[46] Chen X, Lu X-J, Ban Y, et al. Electronic analogy of the Goos–Hänchen effect: a review. J Opt 2013;15:033001.
[47] Li Q, Zhang B, Shen J. Goos-Hänchen shifts of reflected terahertz wave on a COC-air interface. Opt Express 2013;21:6480–7.
[48] Zang M, He T, Zhang B, et al. Temperature-dependent Goos–Hänchen shift in the terahertz range. Opt Commun 2016;370:81–4.
[49] Wang W, Zhang B, Ji H, et al. Terahertz spatial-shift modulation by photo-excitation of polymer/silicon hybrid structures. Opt Commun 2018;421:110–4.
[50] Wu F, Qi X, Qin M, et al. Momentum mismatch driven bound states in the continuum and ellipsometric phase singularities. Phys Rev B 2024;109:085436.
[51] Kühner L, Wendisch FJ, Antonov AA, et al. Unlocking the out-of-plane dimension for photonic bound states in the continuum to achieve maximum optical chirality. Light Sci Appl 2023;12:250.
[52] Artmann K. Berechnung der Seitenversetzung des totalreflektierten Strahles. Annalen der Physik 1948;437:87–102.
[53] Wang L-G, Zhu S-Y. Giant lateral shift of a light beam at the defect mode in one-dimensional photonic crystals. Opt Lett 2006;31:101–3.